ISSN 1674-1056
http://cpb.iphy.ac.cn
http://iopscience.iop.org/cpb
中国物理 B
Chinese Physics
中国物理 Chinese Physics B

Numerical study on magneto-Rayleigh-Taylor instabilities for thin liner implosions on the primary test stand facility

Xiao-Guang Wang(王小光), Shun-Kai Sun(孙顺凯), De-Long Xiao(肖德龙), Guan-Qiong Wang(王冠琼), Yang Zhang(张扬), Shao-Tong Zhou(周少彤), Xiao-Dong Ren(任晓东), Qiang Xu(徐强), Xian-Bin Huang(黄显宾), Ning Ding(丁宁), Xiao-Jian Shu(束小建)

Citation: Chin. Phys. B . 2019, 28(3): 035201. **doi:** 10.1088/1674-1056/28/3/035201
Journal homepage: http://cpb.iphy.ac.cn; http://iopscience.iop.org/cpb

What follows is a list of articles you may be interested in

Observation of double pseudowaves in an ion-beam-plasma system

Zi-An Wei(卫子安), Jin-Xiu Ma(马锦秀), Kai-Yang Yi(弋开阳)
Chin. Phys. B . 2018, 27(8): 085201. **doi:** 10.1088/1674-1056/27/8/085201

Energetic-ion excited internal kink modes with weak magnetic shear in q_0 >1 tokamak plasmas

Wen-Ming Chen(陈文明), Xiao-Gang Wang(王晓钢), Xian-Qu Wang(王先驱), Rui-Bin Zhang(张瑞斌)
Chin. Phys. B . 2017, 26(8): 085201. **doi:** 10.1088/1674-1056/26/8/085201

End-on x-ray backlighting experiments for axial diagnostics of wire-array Z-pinch plasma on PPG-1

Shen Zhao(赵屾), Xinlei Zhu(朱鑫磊), Huantong Shi(石桓通), Xiaobing Zou(邹晓兵), Xinxin Wang(王新新)
Chin. Phys. B . 2017, 26(1): 015206. **doi:** 10.1088/1674-1056/26/1/015206

Effect of shear equilibrium flow in Tokamak plasma on resistive wall modes

Li Li, Liu Yue
Chin. Phys. B . 2013, 22(7): 075203. **doi:** 10.1088/1674-1056/22/7/075203

Blockage effects on viscous fluid flow and heat transfer past a magnetic obstacle in a duct

Zhang Xi-Dong, Huang Hu-Lin
Chin. Phys. B . 2013, 22(7): 075202. **doi:** 10.1088/1674-1056/22/7/075202

Numerical study on magneto-Rayleigh–Taylor instabilities for thin liner implosions on the primary test stand facility*

Xiao-Guang Wang(王小光)[1], Shun-Kai Sun(孙顺凯)[1], De-Long Xiao(肖德龙)[1,†], Guan-Qiong Wang(王冠琼)[1], Yang Zhang(张扬)[1], Shao-Tong Zhou(周少彤)[2], Xiao-Dong Ren(任晓东)[2], Qiang Xu(徐强)[2], Xian-Bin Huang(黄显宾)[2], Ning Ding(丁宁)[1], and Xiao-Jian Shu(束小建)[1]

[1] *Institute of Applied Physics and Computational Mathematics, Beijing* 100088, *China*
[2] *Institute of Fluid Physics, China Academy of Engineering Physics, Mianyang* 621999, *China*

(Received 8 October 2018; revised manuscript received 7 January 2019; published online 22 February 2019)

The thin aluminum liners with an aspect ratio $R/\Delta r \ll 1$ have been imploded on the primary test stand (PTS) facility, where R is the outer radius of the liner and Δr is the thickness. The x-ray self-emission images present azimuthally correlated perturbations in the liner implosions. The experiments show that at -10 ns before the stagnation, the wavelengths of perturbation are about 0.93 mm and 1.67 mm for the small-radius and large-radius liners, respectively. We have utilized the resistive magnetohydrodynamic code PLUTO to study the development of magneto-Rayleigh–Taylor (MRT) instabilities under experimental conditions. The calculated perturbation amplitudes are consistent with the experimental observations very well. We have found that both mode coupling and long implosion distance are responsible for the more developed instabilities in the large-radius liner implosions.

Keywords: magneto-Rayleigh–Taylor instability, thin liner implosion, *Z*-pinches, magnetohydrodynamic (MHD), primary test stand (PTS)

PACS: 52.30.Cv, 52.35.–g, 52.58.Lq, 52.65.Kj **DOI:** 10.1088/1674-1056/28/3/035201

1. Introduction

In implosions of cylindrical *Z*-pinches driven by magnetic field, magneto-Rayleigh–Taylor (MRT) instability will occur at the outer plasma–vacuum interface, where the plasma liner (heavy fluid) is accelerated by azimuthal magnetic field (light fluid) analogous to classical fluid Rayleigh–Taylor (RT) instability.[1–5] In addition to acceleration, the effective gravity resulting from the curvature and gradient of magnetic field could also contribute to the growth of instability,[4,6,7] i.e., MRT-like sausage mode, which is one of the distinctive features from the RT instability. The imploding cylindrical plasma would be broken up by the fully developed MRT instability, so that it does not reach the axis in an intact state.[8–10] Thus, all applications of fast *Z*-pinches are sensitive to the instability.

Large amounts of experimental and numerical works have already been done on the MRT instability for decades.[1,7,11–20] Both two-dimensional (2D) and three-dimensional (3D) radiative magnetohydrodynamic (MHD) simulations could reproduce the experimental radiation pulse very well by self-consistently considering the instability.[18,21,22] Besides the wire array, the liner (or cylindrical foil) is an alternative load to *Z*-pinch applications. But it is found from experiments that thin liners were more susceptible to the MRT instability than the wire array because of the earlier implosion and the initial coherent perturbation, resulting in lower x-ray radiation power.[23] The MRT instabilities also appeared in the planar foil implosion experiments.[24]

In order to decrease the effect of MRTs, thick solid liners with an aspect ratio $R/\Delta r \sim 6$ were utilized to compress pre-magnetized and pre-heating deuterium plasma in magnetized liner inertial fusion (MagLIF).[25,26] The liner implosion experiments with initial single mode perturbation were performed on the *Z* machine for the MRT instability study, where the measured mode growth in the implosion phase was in agreement with numerical and theoretical results very well.[27–29] Numerical simulations showed that the outer surface of liner was disturbed by the MRT instability, but the inner surface would keep intact because of the liner's sufficiently thick shell.[29] Recently, thin foil (of 400 nm thickness) implosion experiments demonstrated that the applied axial magnetic field generated the helical structure MHD and MRT instabilities, and reduced the perturbation amplitude.[30,31] The inverse cascades in both the axial and azimuthal wavenumbers were observed in these experiments. Extended MHD simulation suggested that the flux compression of the applied magnetic field by the outer low-density plasma may be a possible reason for the large pitch angle of the helical perturbation observed in liner experiments on the *Z* facility.[32]

In this article, the non-magnetized thin aluminum liners with $R/\Delta r = 3200$ and 5000 were imploded on the primary test stand (PTS) facility[33] with a peak current of 6.4–8.0 MA and rising time (10%–90%) of 60–70 ns. Azimuthally correlated

*Project supported by the National Natural Science Foundation of China (Grant Nos. 11605013, 11775032, 11805019, and 11705013).
†Corresponding author. E-mail: xiao_delong@iapcm.ac.cn
© 2019 Chinese Physical Society and IOP Publishing Ltd

perturbations appeared in the implosions, which are believed to be the consequence of MRT instabilities. In order to understand the experiments, we utilized a resistive MHD code to investigate the MRT instability development. The instability grew exponentially even in the nonlinear phase,[6,29,34] possibly leading to fully developed mode coupling.[35] The strong mode coupling would contribute to the growth of the long wave modes very much. In Douglas' computation, the strong mode coupling was observed clearly between modes with $\lambda \geqslant \Delta r$, where λ is the wavelength.[34] In general, the mode would develop stronger for the large-radius liner because of the longer implosion distance. Both longer implosion distance and strong mode coupling may be responsible for the more developed MRT in the large-radius liner implosion than the small-radius one.

Section 2 introduces the physical models for cylindrical liner implosions. The numerical effects on the growth of the instability are discussed in Section 3. The experimental results are presented, and the single mode, two-mode coupling, and random seed developments are studied under the experimental conditions by simulation in Section 4. Finally, Section 5 gives the conclusions.

2. Physical models

We will only take the axial magneto-Rayleigh–Taylor instability (in $R-Z$ cross section) into account here, because it is more dangerous for the implosion of a cylindrical liner driven by an azimuthal magnetic field. Moreover, the cylindrical coordinate system is applied due to its cylindrical symmetry in this paper. We focus on the MRTs in the run-in phase of the liner implosion. Ignoring the liner-initiation phase, a plasma shell with finite temperature and density is taken as the initial conditions in our computations.[2,21,36] Figure 1 shows the $R-Z$ cross section schematic diagram for the cylindrical configuration. We set the azimuthal magnetic field at the outer boundary

$$B_{\theta \mathrm{b}} = \frac{2}{c}\frac{I(t)}{R_{\mathrm{b}}} \tag{1}$$

as the driving source, where $I(t)$ is the driven current, R_{b} is the radius of the outer boundary, and c is the speed of light in vacuum. The compressible resistive magnetohydrodynamic control equations include the continuity equation, the momentum equation, the energy equation, and the magnetic field equation, which are written into the conservative form as follows:[37]

$$\frac{\partial \rho}{\partial t} + \nabla \cdot (\rho \boldsymbol{v}) = 0, \tag{2}$$

$$\frac{\partial \boldsymbol{m}}{\partial t} + \nabla \cdot \left(\boldsymbol{m}v + \frac{1}{4\pi}\boldsymbol{B}\boldsymbol{B} + \overleftrightarrow{I} p_{\mathrm{t}}\right) = 0, \tag{3}$$

$$\frac{\partial E}{\partial t} + \nabla \cdot [(E + p_{\mathrm{t}})\boldsymbol{v} - \boldsymbol{B}(\boldsymbol{v} \cdot \boldsymbol{B})] = -\nabla [(\eta \cdot \boldsymbol{J}) \times \boldsymbol{B}] + \nabla \cdot \boldsymbol{F}_{\mathrm{c}}, \tag{4}$$

$$\frac{\partial \boldsymbol{B}}{\partial t} + \nabla \times (-\boldsymbol{v} \times \boldsymbol{B}) = -\nabla \times (\eta \cdot \boldsymbol{J}), \tag{5}$$

where ρ is the mass density, $\boldsymbol{m} = \rho \boldsymbol{v}$ is the momentum, $\boldsymbol{v}$ is the velocity, $p_{\mathrm{t}} = p + \boldsymbol{B}^2$ is the total pressure, p is the thermal pressure, $\boldsymbol{B}$ is the magnetic field, $\boldsymbol{J} = \nabla \times \boldsymbol{B}$ is the current density, and η is the resistivity. E is the total energy

$$E = \rho e + \frac{\boldsymbol{m}^2}{2\rho} + \frac{\boldsymbol{B}^2}{8\pi}. \tag{6}$$

The limited energy flux is utilized in the energy equation

$$\boldsymbol{F}_{\mathrm{c}} = \frac{F_{\mathrm{sat}}}{F_{\mathrm{sat}} + |F_{\mathrm{class}}|}\boldsymbol{F}_{\mathrm{class}}, \tag{7}$$

where $\boldsymbol{F}_{\mathrm{class}} = \kappa_{\mathrm{par}}\hat{b}\left(\hat{b} \cdot \nabla T\right) + \kappa_{\mathrm{per}}\left[\nabla T - \hat{b}\left(\hat{b} \cdot \nabla T\right)\right]$ is the classical energy flux, T is the temperature, and κ_{par} and κ_{per} are the parallel and normal heat conductivity coefficients, respectively.

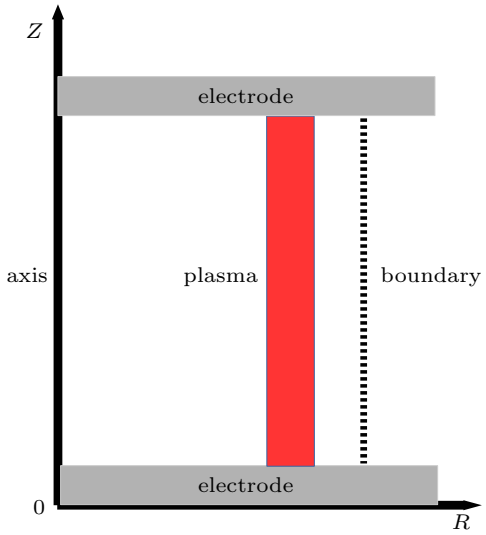


Fig. 1. The $R-Z$ cross-section schematic diagram of the cylindrical Z-pinch load configuration in simulations.

The partially ionized ideal gas equation of state is used to provide the closure

$$\begin{aligned} p &= \rho / m_{\mathrm{A}} (1 + Z_{\mathrm{eff}}) T, \\ e &= (1 + Z_{\mathrm{eff}}) T / m_{\mathrm{A}} + I_{\mathrm{TF}} / \rho, \end{aligned} \tag{8}$$

where

$$I_{\mathrm{TF}} = 13.6 \times Z_{\mathrm{atom}}^{4/3} \frac{(Z_{\mathrm{eff}}/Z_{\mathrm{atom}})^2}{(1 - Z_{\mathrm{eff}}/Z_{\mathrm{atom}})^{3/2}} \tag{9}$$

is the Thomas–Fermi ionization potential,[38] Z_{atom} is the atomic number of the material (aluminum here), m_{A} is the atomic mass, and Z_{eff} is the average degree of ionization, calculated by the Thomas–Fermi ionization model.[38] The Braginskii heat conductivity coefficients and the Spitzer resistivity are employed here. In the run-in phase of the liner implosion, as shown in Fig. 6, the hydrodynamic energy is much larger than the radiation energy. In addition, we did not find substantial effects on the results by adding a black body radiation term in the energy equation. Therefore, the radiation is ignored in this phase here.

The experimental and computational results in Peterson's paper showed that the electro-thermal instability appearing in the initial phase may be the mechanism of seeding the MHD and MRT instability in the liner implosion. However, the seeding of the MHD and MRT instabilities is still an open problem, which is beyond the scope of this paper. Therefore, we study the MRT instability only in the run-in phase of the liner implosion. The initial condition of the liner is considered as a plasma shell with higher temperature and lower density than the solid. The MRT instability is seeded by cosine or random density perturbation. The resistive MHD code PLUTO,[37] which is employed widely in astrophysics, is utilized to solve the above control equations.

3. Numerical effects

First, we compare the computational results with Ref. [34] to validate the modified PLUTO for studying MRT instabilities in the Z-pinch implosions. The cosine function

$$\xi = \delta_0 \rho_0 \times \cos\left(n\frac{Z}{l}2\pi\right) \tag{10}$$

is chosen as the initial perturbation for single mode development, where n is the mode number in the Z direction, δ_0 is the perturbation amplitude, and l is the length of plasma shell. The same parameters and driven current in Ref. [34] are used for comparison, where the peak current is about 16 MA and the implosion time is about 100 ns. The height of plasma shell $l = 2$ cm, and its initial radius $R_0 = 2$ cm. The initial thickness of the plasma shell is $\Delta r = 0.1$ cm. The initial density ρ_0 and temperature T_0 of the plasma shell are spatially uniform. The initial perturbation with $\delta_0 = 0.005$ is utilized. In addition, the same cell numbers, i.e., 5 cells/mm in the R direction and 8 cells/mm in the Z direction, are also used in this section. Analogous to Refs. [31] and [35], we analyze the spectrum by calculating the radial density integral and subtracting its mean

$$\begin{aligned} H(Z) &= \frac{\left(\int \rho(R,Z) R \mathrm{d}R\right) - \bar{H}}{\rho_{\max} R_{\mathrm{mc}}}, \\ \bar{H} &= \frac{\int \rho(R,Z) R \mathrm{d}R \mathrm{d}Z}{\int \mathrm{d}Z}, \\ R_{\mathrm{mc}} &= \frac{\iint \rho R^2 \mathrm{d}Z \mathrm{d}R}{\iint \rho R \mathrm{d}Z \mathrm{d}R}, \end{aligned} \tag{11}$$

where in order to obtain a quantity with units of length, we divide the density integral by the max density $\rho_{\max} = \max\left[\int \rho(R,Z)\,\mathrm{d}Z/l\right]_R$ and the radius of the center of mass R_{mc}. The growth rate γ is obtained by fitting the computational amplitude with exponential function $\eta_0 \exp(\gamma t)$.[34] The spectra of single mode $n = 8$ are presented at four different times in Fig. 2. The ratio of Δr to λ approaches to unit for this mode. The growth rate by fitting the computational mode amplitudes between 160 ns and 200 ns is about $\gamma = 0.120$/ns for the mode $n = 8$. The physical picture and growth rate are both consistent with MACH2's results.[34] Moreover, the PLUTO results of two-mode coupling and random seed development are also consistent with Ref. [34].

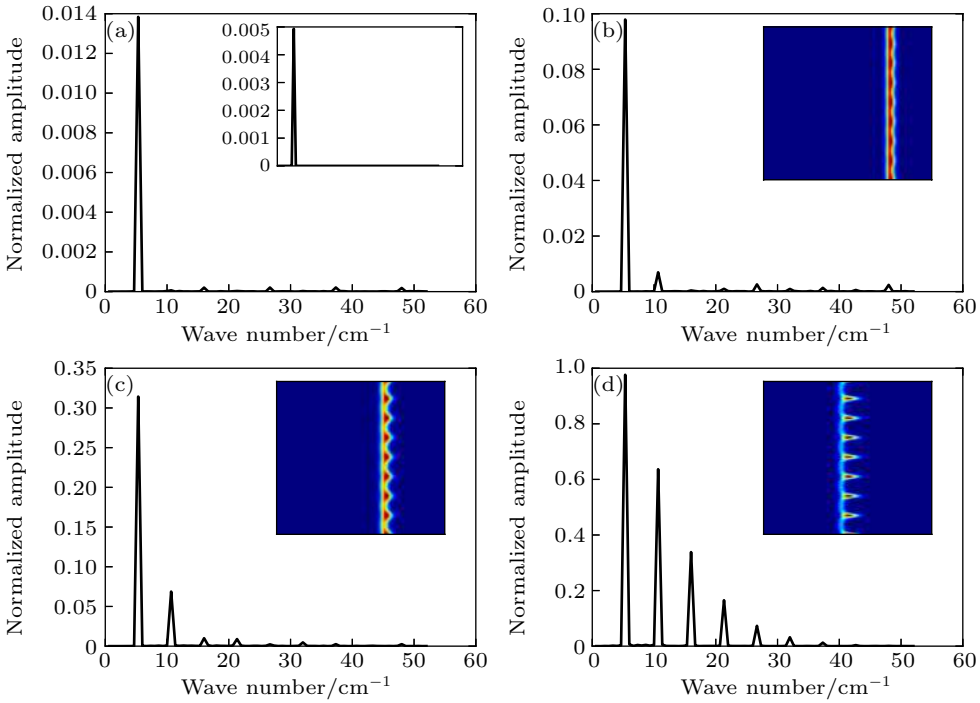


Fig. 2. Compared with Ref. [34], wave spectrum of mode $n = 8$ at $t =$ (a) 170 ns, (b) 190 ns, (c) 200 ns, and (d) 210 ns. The inset in (a) is the initial wave spectrum, and the insets in (b)–(d) show density distribution.

Then, different cell numbers are employed for determining numerical effects on the growth of the instability. In Fig. 3, the growth rates of mode $n = 8$ as a function of the cell number per wavelength in the Z direction are presented for two different cell numbers in the R direction respectively. It is found that the numerical dissipation due to finite cells, analogous to physical viscosity, will decrease the instability growth rate.[34] More than 10 cells per wavelength in the Z direction are required for the single mode MRT instability study. In addition, the computational results approach convergence when the cell number reaches 25 per millimeter in the R direction, as shown in Fig. 3.

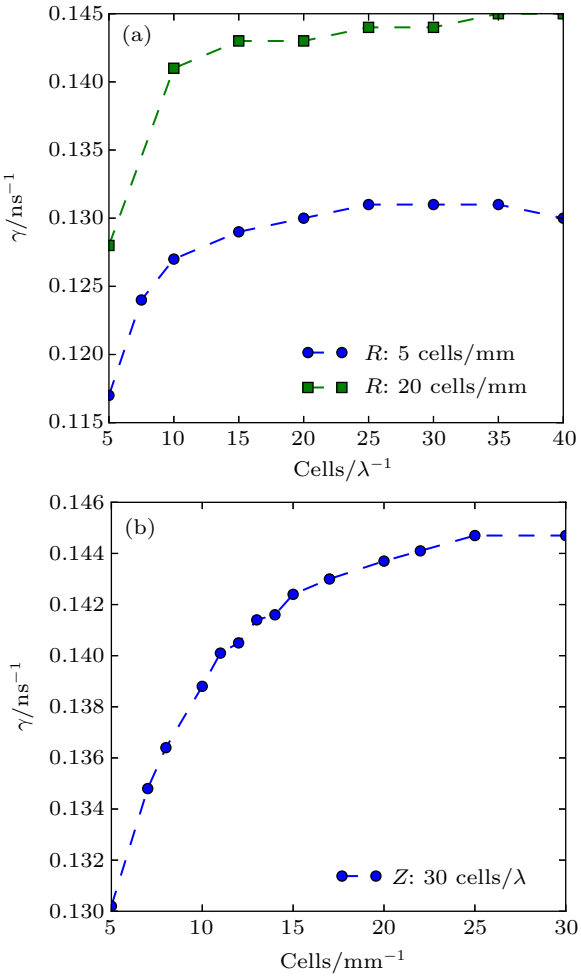


Fig. 3. Linear growth rate of mode $n = 8$ (a) as a function of cell number per wavelength in the Z direction for two different cell numbers in the R direction and (b) as a function of cell number in the R direction for 30 cells per wavelength in the Z direction.

4. Results

4.1. Experimental results

The thin liners with $R/\Delta r = 3200$ and 5000 were imploded with a peak current of 6.4–8.0 MA and rising time (10%–90%) of 60–70 ns on the PTS facility. The liners were fabricated by rolling up a rectangular aluminum foil (of 2 μm thickness), with one end sticking to the electrodes. For the small-radius liner ($R/\Delta r = 3200$), the radius is $R = 0.64$ cm, the thickness is $\Delta r = 2.0$ μm, and the height is $l = 1.5$ cm. Its line mass is 2.20 mg/cm. For the large-radius liner ($R/\Delta r = 5000$), $R = 1.0$ cm, $\Delta r = 2.0$ μm, and $l = 1.5$ cm. Its line mass is 3.43 mg/cm. The primary diagnostics to investigate the implosion dynamics of the liners are the x-ray pinhole cameras and the laser shadowgraphy.[39] One x-ray pinhole camera is used with 6 μm Mylar filter paired with multilayer mirror to produce integrated monochromatic (277 ± 5 eV) framing images (see Figs. 4 and 5). The frequency-doubled Nd:YAG laser (532 nm) was used to produce laser shadowgraph (see Figs. 4 and 5) with the time interval 6 ns between images. In addition, the filtered x-ray diode (XRD) was used to measure the soft x-ray power.

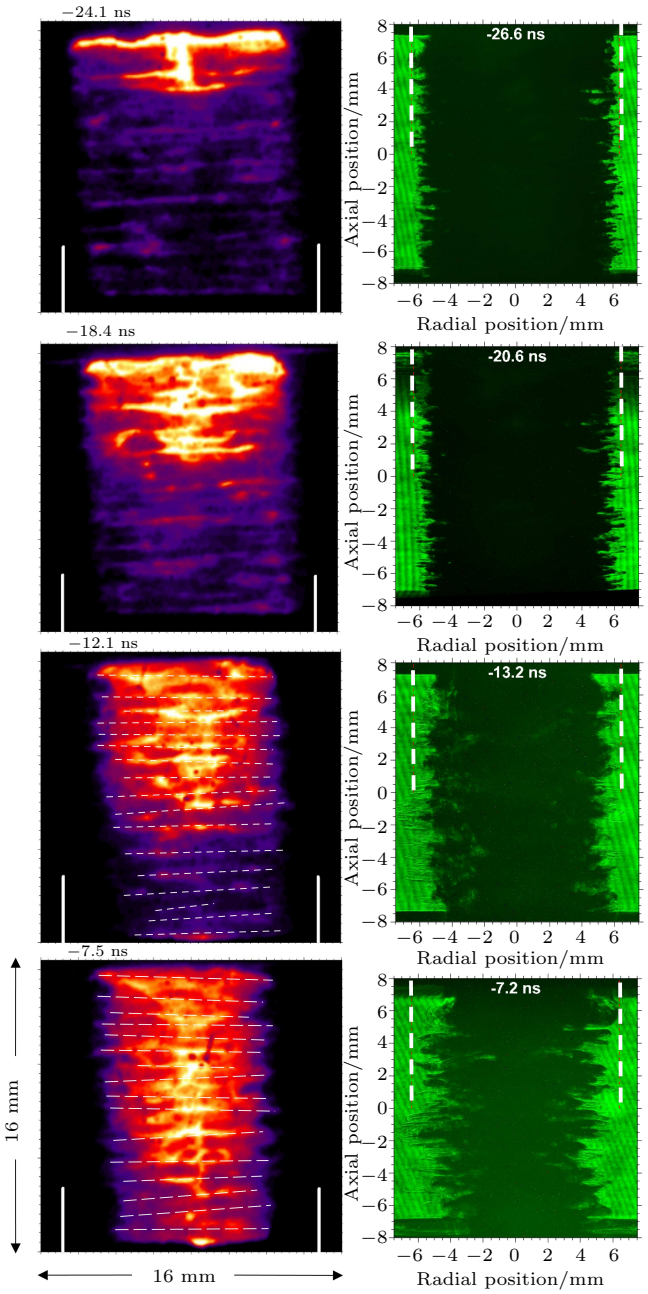


Fig. 4. The x-ray self-emission images (left) and laser shadowgraphs (right) for the small-radius liner implosion (shots 0319, 0318, and 0316). The vertical white lines indicate the initial position of the liner.

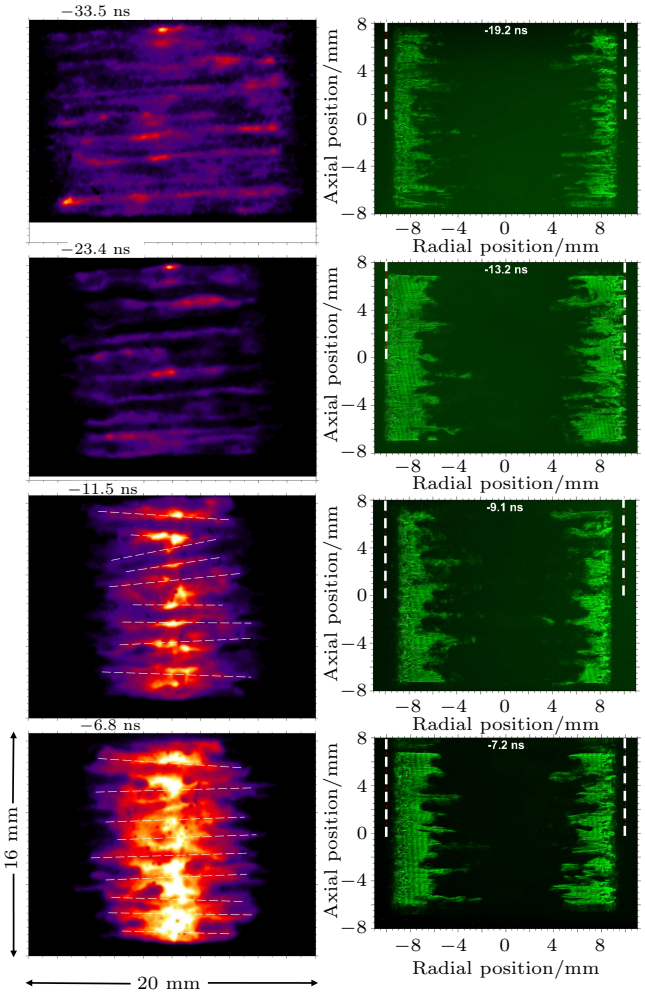


Fig. 5. The x-ray self-emission images (left) and laser shadowgraphs (right) for the large-radius liner implosion (shots 0320–0322). The vertical white lines indicate the initial position of the liner. The initial position is at the left and right edges of the x-ray images.

Figures 4 and 5 show the monochromatic x-ray self-emission images and laser shadowgraphs at different times for the small- and large-radius liner implosions, respectively. The $t = 0$ time is defined at the peak radiation power in experiments. The x-ray figures show azimuthally coherent stratifications, which are believed to be the consequence of MRT instabilities. For the small-radius and large-radius liner implosions, the dominant perturbation wavelengths are about 0.93 mm and 1.67 mm around −10 ns. It is found that, from Figs. 4 and 5, both the perturbation amplitude and dominant wavelength for the large-radius liner are larger than the small-radius one. In addition, the laser shadowgraph images present clearly the inversed cascade phenomenon before the stagnation.

In order to understand the experiments, we have simulated the single mode development, two-mode coupling, and random seed development under the experimental conditions.

4.2. Single mode development

In our simulation, the measured load current from shot #0317, with peak current of 6.6 MA and rising time of 64 ns, is used as the driven current for the liner $R/\Delta r = 3200$ (small-radius liner). We take a plasma shell as the initial condition in calculations. The outer radius of the plasma shell is 0.64 cm. The height is 1.5 cm. In experiments, a radiation ring of width ~ 0.1 cm appears inside $r = 5$ mm (the radius of the diagnostic hole) in the end-on x-ray images at ~ -40 ns in the run-in phase for the small-radius liner. According to this phenomenon and the previous calculation works,[34] the initial thickness of plasma shell is set as 0.10 cm. The initial density is 5.93 mg/cm^3 to keep the same line mass with experiments. A low temperature 2.3×10^3 K is set for mitigating the influence of plasma expansion before the liner implosion. In the same way, the measured load current from shot #0321, with peak current of 7.8 MA and rising time of 70 ns, is used for the liner $R/\Delta r = 5000$ (large-radius liner). The outer radius of plasma shell is 1.0 cm and the thickness is 0.1 cm. The initial temperature of plasma shell is 2.4×10^3 K, and the initial density is 5.70 mg/cm^3. The initial density perturbations ξ with $\delta_0 = 0.005$ are used for the two kinds of liners. More than 20 cells/mm are employed in our computation according to Section 3.

For comparison with experiments, $t = 0$ is defined when the kinetic energy is minimum in the computation. In experiments, the $t = 0$ time is defined when the radiation power is peak. The time of the minimum kinetic energy in calculation is consistent with that of the peak radiation power in experiments for the small-radius liner implosion, as shown in Fig. 6. This is the same result for the large-radius liner implosions.

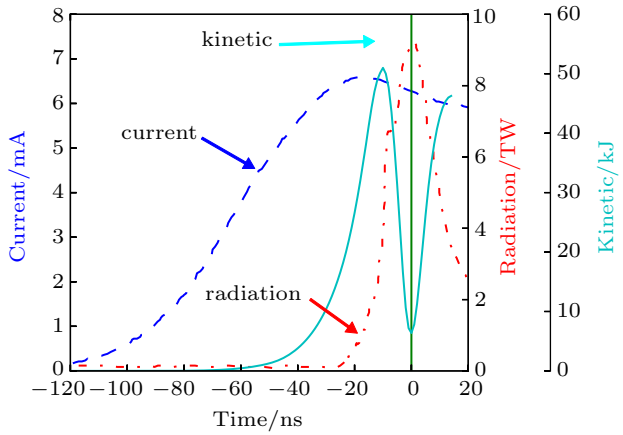


Fig. 6. Experimental (shot 0317) current (dashed line) and radiation power (dot-dashed line) as a function of time are plotted for the small-radius liner implosion as well as the calculated kinetic energy (solid line).

We compare the computational results with the linear theory, which is consistent with the thick liner ($R/\Delta r \sim 6$) implosion experiments on the Z machine.[6,29] The exponential law, $\eta = \eta_0 \cosh[G_s(t)]$, is employed to describe the growth of MRT instability in linear theory,[29] where $G_s(t) = \int_0^t \gamma(t')\,\mathrm{d}t'$, and $\gamma = \sqrt{kg}$. The acceleration is calculated from the magnetic pressure

$$g(t) = -\frac{\mu_0}{4\pi m_L}\frac{I^2(t)}{R_{mc}(t)}, \tag{12}$$

where $R_{mc}(t)$ is the radius at the center of mass from numerical results and m_L is the line mass.

Corresponding to the small-radius liner implosion, figure 7 presents the computational mode amplitude (Fourier analysis, fast Fourier transform (FFT)), valley–peak length, and the exponential growth law in logarithmic coordinate as a function of time for single modes $n = 8$ ($\lambda \sim 1.9$ mm) and $n = 15$ ($\lambda \sim 1.0$ mm). Figure 8 is for the large-radius liner implosion. The computational results show that the amplitude of MRT instability will decrease before the start of the implosion because of the expansion of the outer face. The single mode MRT grows exponentially in the run-in phase. Furthermore, the growth of MRT in the computation is faster than that predicted by linear theory after -40 ns for small-radius liner and -70 ns for large-radius liner, as shown in Figs. 7 and 8, which is different from the thick liner with $R/\Delta r \sim 6$.[27–29] Similar results are also found for mode $n = 20$ ($\lambda \sim 0.75$ mm), the wavelength of which is smaller than the initial plasma thickness, in both kinds of liner implosions. One possible reason is that $g(t)$, which is calculated from the radius of the center of mass and the magnetic pressure, may be underestimated for the mode growth. In addition, the perturbation amplitude is larger for the large-radius liner than the small-radius before stagnation because of the longer implosion distance. This is consistent with the experimental observation.

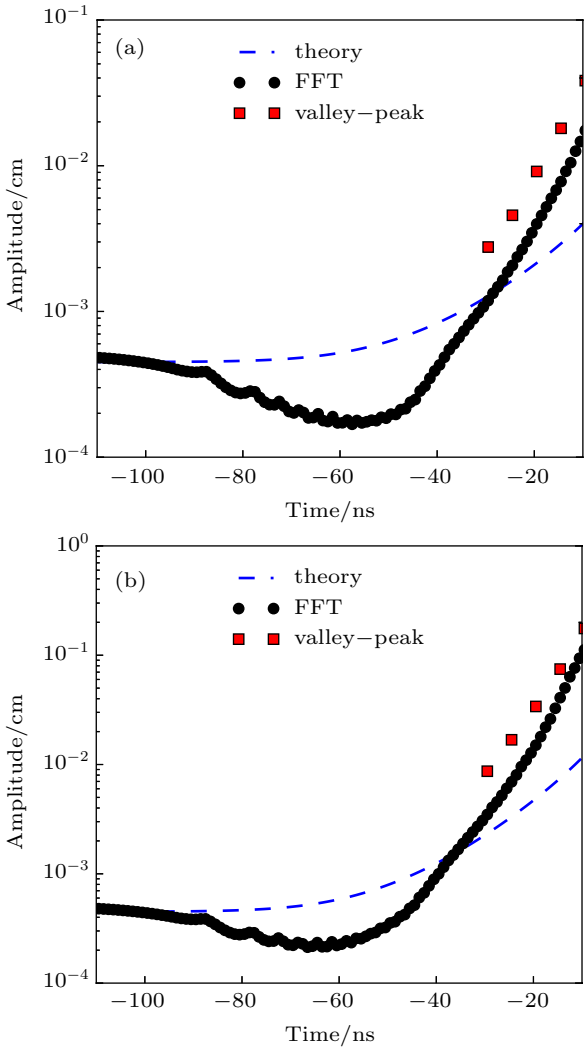


Fig. 7. Corresponding to the small-radius liner implosion experiments, the computational mode amplitude (solid circle), the valley-peak length (solid square), and the theoretical result (dashed line) are presented as a function of time for single modes (a) $n = 8$ ($\lambda \sim 1.9$ mm) and (b) $n = 15$ ($\lambda \sim 1.0$ mm).

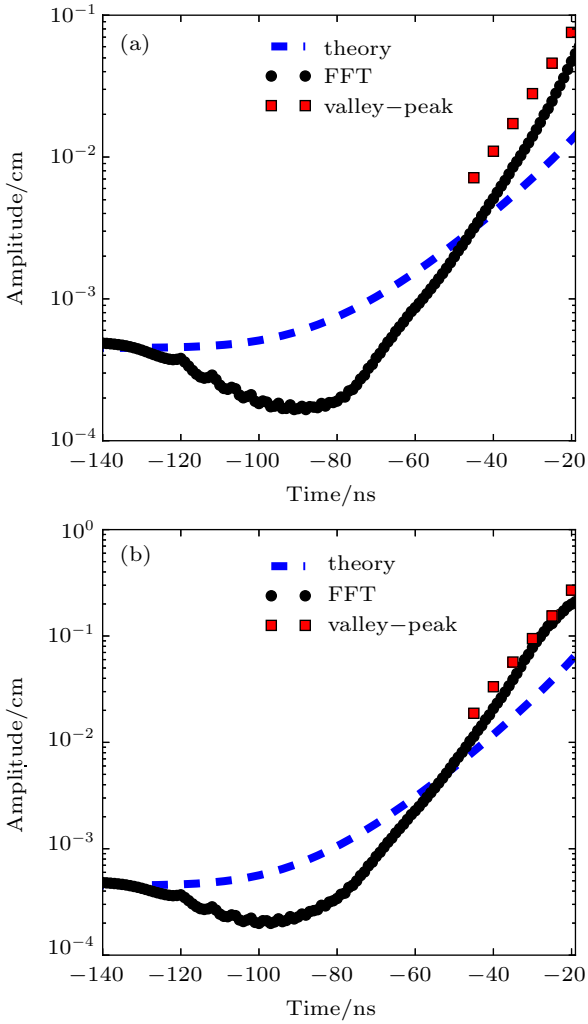


Fig. 8. Corresponding to the large-radius liner implosion experiments, the computational mode amplitude (solid circle), the valley-peak length (solid square), and the theoretical result (dashed line) are presented as a function of time for single modes (a) $n = 8$ ($\lambda \sim 1.9$ mm) and (b) $n = 15$ ($\lambda \sim 1.0$ mm).

4.3. Two-mode coupling

With other parameters corresponding to Section 4.2, two single mode seeds $n = 8(k_1)$ and $12(k_2)$ with $\delta_0 = 0.005$ are respectively imposed on the plasma liner together for the small- and large-radius liner implosions. There is no initial phase difference between the two modes. It is seen from Fig. 9 that modes $n = 4(k_2 - k_1)$ and $n = 20(k_2 + k_1)$ are generated by mode coupling and grow as the plasma implodes. The generated mode $n = 20$ grows even larger than the mode $n = 8$ before stagnation. It is found that the growth rate of $n = 4$ is larger than modes $n = 8$ and $n = 12$ by fitting the amplitude with $\eta_0 \exp(\gamma t)$. It is seen from Fig. 9(b) that the mode $n = 12$ and the second harmonic mode $n = 16$ begin to "saturate" and decrease before stagnation for the large-radius liner. However, this phenomenon is not found in the small-radius liner implosion. It implies stronger mode coupling for the large-radius liner. In fact, the "saturation" and decreasing also occur in the

simulation of two-mode coupling under the Z machine experimental conditions as in Section 3, where R and $R/\Delta r$ are larger and the implosion time is shorter. It is deduced that the mode coupling is stronger for larger radius or $R/\Delta r$. According to the quasi-linear mode coupling theory,[35,40] mode coupling will contribute to the long wave mode and make it grow faster. This may be also responsible for the more developed MRT observed in large-radius liner experiments.

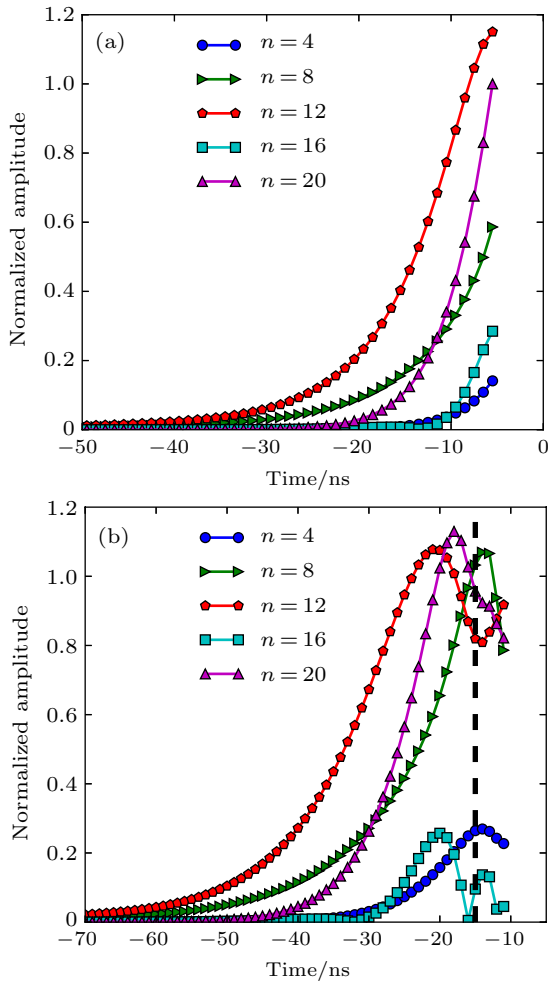


Fig. 9. Different mode amplitudes from $n=8$ and $n=12$ mode coupling are presented as a function of time for the (a) small- and (b) large-radius liners, respectively. The stagnation begins after -15 ns as the vertical dash line indicates in (b).

4.4. Random seed development

With other parameters corresponding to Section 4.2, we also apply random density perturbation seed

$$\tilde{\rho} = \delta_0 \rho_0 \text{Random}(-1.0, 1.0) \tag{13}$$

for the MRT instability study, where δ_0 is the perturbation amplitude and ρ is the unperturbed density. The initial temperature is 10^4 K here. According to Section 3, 35 cells/mm in the R direction and 20 cells/mm in the Z direction ($l=15$ mm) are employed for lowering the effect of numerical dissipation on the observed dominant modes as much as possible. And the initial amplitude $\delta_0 = 0.05$ is chosen in the computation.

Figure 10 shows the density distribution and the corresponding wave spectrum at -10 ns for the small-radius liner implosion, while figure 11 is for the large-radius liner. Analogous to experiments, it is found that the perturbation amplitude and wavelength are both larger for the large-liner than the small-radius one, as shown in Figs. 10 and 11. From the perturbation spectrum, it is found that in our computation, the dominant mode wavelengths are ~ 0.9 mm and ~ 2.0 mm for the small-radius and large-radius liner implosion, respectively, which is in agreement with the experimental observation. The same initial amplitudes are applied for the two kinds of liner implosions. More than three calculations are done for each case, obtaining the average results.

Figure 12 presents the measured and computational perturbation amplitudes for the liner $R/\Delta r = 3200$. In experiments, the amplitude is measured by the maximum distance between the finger peak and bubble valley of the laser shadowgraph. In calculations, the amplitude is calculated by the maximum distance between the finger peak and bubble valley of the density contour map. The calculated amplitudes are consistent with the experimental results very well.

Corresponding to Figs. 10 and 11, respectively, figures 13 and 14 present the perturbation amplitudes of different modes

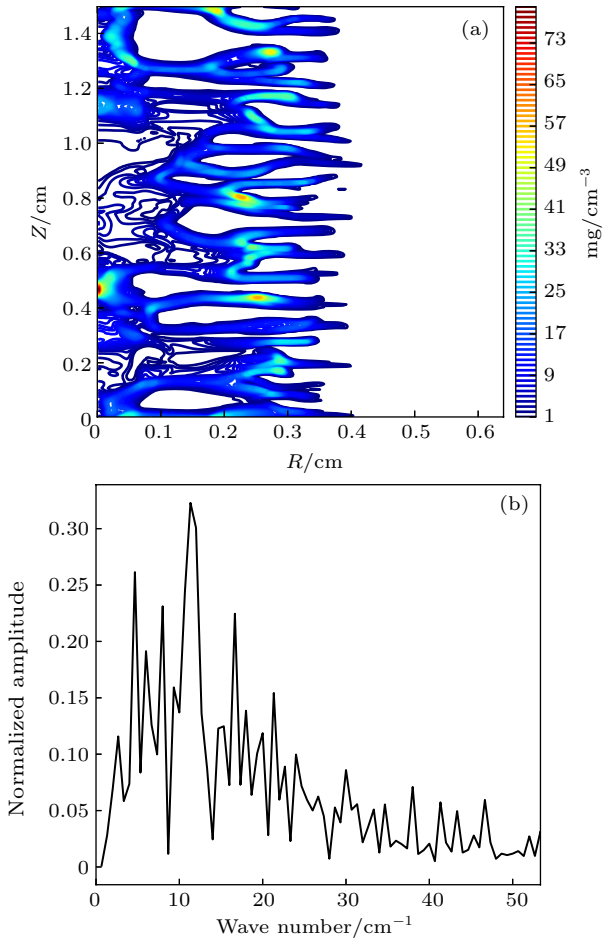


Fig. 10. Corresponding to the small-radius liner, the (a) density distribution contour and (b) wave spectrum are presented at $t=-10$ ns.

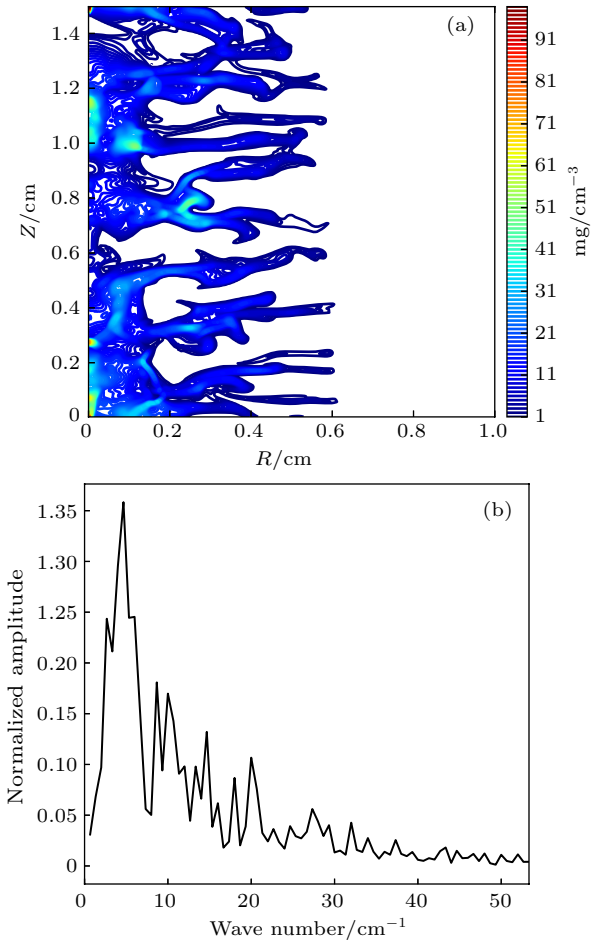


Fig. 11. Corresponding to the large-radius liner, the (a) density distribution contour and (b) wave spectrum are presented at $t = -10$ ns.

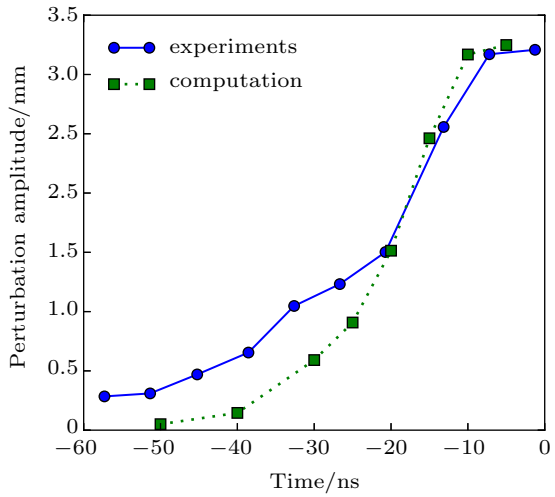


Fig. 12. The measured and computational perturbation amplitudes for the small-radius liner ($R/\Delta r = 3200$).

as a function of time. The wavelength of the dominant mode increases with time as shown in Figs. 13 and 14, which corresponds to the inversed cascade phenomena in experiments. Compared with Fig. 9, richer mode couplings are presented for random seeds than simple two-mode seeds. The competition between the mode growth and the mode coupling should be responsible for the mode amplitude bouncing (the growth–decrease–growth process) observed in Figs. 13 and 14. Obviously, the MRT mode experiences the growth–decrease–growth process more times for the large-radius than the small-radius liner, which indicates more fully developed mode coupling. Referring to Ofer[35] and Haan,[40] it is known that strong mode coupling would contribute to the long wave mode growth. Therefore, more perturbation energy is fast transported to the long wavelength mode by mode coupling. It is consistent with the results of Section 4.2. Consequently, more fully developed mode coupling is another possible reason for the larger perturbation amplitude and wavelength of the instabilities in large-radius liner implosion in addition to the longer implosion distance.

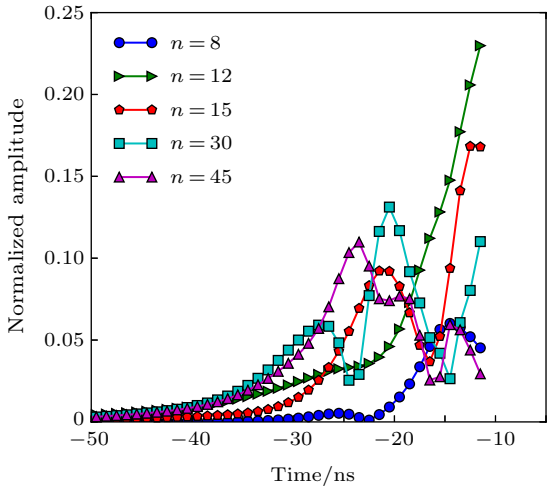


Fig. 13. Corresponding to Fig. 10, the amplitudes of different modes as a function of time are presented.

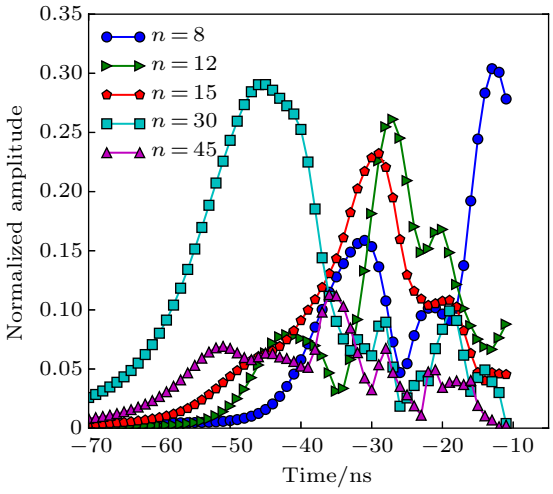


Fig. 14. Corresponding to Fig. 11, the amplitudes of different modes as a function of time are presented.

5. Conclusion

The liner implosion experiments with $R/\Delta r \ll 1$ are performed on the PTS facility for implosion dynamics study. The MRT instabilities are observed in experiments. Both the perturbation amplitude and the dominant wavelength are found to be larger in the large-radius than the small-radius liner from x-ray self-emission images. In order to understand the experiments, resistive MHD code PLUTO is utilized to investigate

the single mode development, two-mode coupling, and random seed development of MRT instability under the experimental conditions.

Firstly, it is found that the single mode growth is faster than that predicted by linear theory before stagnation. In addition, the single mode amplitude for the large-radius liner is larger than the small-radius one because of the longer implosion distance. It is partially responsible for the larger perturbation amplitude and wavelength observed in the large-radius liner implosions.

Our simulations on two-mode coupling and random seed development show that the mode coupling will develop more strongly with larger radius and aspect ratio $R/\Delta r$ (i.e., thinner liner). According to quasi-linear mode coupling theory,[35,40] mode coupling will contribute to the growth of the longer wavelength mode. Therefore, the stronger mode coupling may also be responsible for the more developed MRT instabilities in the large-radius liner implosion. The physical picture from computations for the random perturbation seed is qualitatively consistent with experimental observations. In addition, the wavelengths of the dominant modes are in good agreement with experimental observation.

According to the results above, both the long implosion distance and fully developed mode coupling contribute to the larger perturbation and wavelength of the dominant mode for the large-radius liner implosions. Actually, the large radius and high aspect ratio are unavoidable for some Z-pinch applications especially at large current, such as the dynamic hohlraum and soft x-ray radiation. Therefore, some measures must be taken to alleviate the MRT development and mode coupling before the stagnation or collision with the converter for the thin liner implosion. Analogous to nested wire-arrays and gas puff, the nested liner may be helpful to mitigate the effect of MRT instability. The matched line mass and position of the nested liner should be optimized carefully in future study.

Acknowledgment

The authors thank the experimental teams on the PTS facility from the Institute of Fluid Physics, the Institute of Nuclear Physics and Chemistry, and the Research Center of Laser Fusion of the China Academy of Engineering Physics.

References

[1] Douglas M R, De Groot J S and Spielman R B 2001 *Laser Part. Beams* **19** 527
[2] Peterson D L, Bowers R L, Brownell J H, Greene A E, McLenithan K D, Oliphant T A, Roderick N F and Scannapieco A J 1996 *Phys. Plasmas* **3** 368
[3] Haines M G 2011 *Plasma Phys. Control. Fusion* **53** 093001
[4] Ryutov D D, Derzon M S and Matzen M K 2000 *Rev. Mod. Phys.* **72** 167
[5] Sharp D H 1984 *Phys. D: Nonlinear Phenom.* **12** 3
[6] Miles A R 2009 *Phys. Plasmas* **16** 032702
[7] Weis M R, Zhang P, Lau Y Y, Schmit P F, Peterson K J, Hess M and Gilgenbach R M 2015 *Phys. Plasmas* **22** 032706
[8] Ivanov V V, Sotnikov V I, Sarkisov G, Astanovitskiy A L, Laca P J, Cowan T E, Jones B, Deeney C, Oliver B V, Mehlhorn T A and Leboeuf J N G 2007 *IEEE Trans. Plasma Sci.* **35** 1170
[9] Ivanov V V, Chittenden J P, Altemara S D, Niasse N, Hakel P, Mancini R C, Papp D and Anderson A A 2011 *Phys. Rev. Lett.* **107** 165002
[10] Chittenden J P and Jennings C A 2008 *Phys. Rev. Lett.* **101** 055005
[11] Sun Y B and Piriz A R 2014 *Phys. Plasmas* **21** 072708
[12] Huang B, Tomizuka T, Xie B, Sakai Y, Zhu Q, Song I, Okino A, Xiao F, Watanabe M and Hotta E 2013 *Phys. Plasmas* **20** 112113
[13] Zhang P, Lau Y Y, Rittersdorf I M, Weis M R, Gilgenbach R M, Chalenski D and Slutz S A 2012 *Phys. Plasmas* **19** 022703
[14] Lau Y Y, Zier J C, Rittersdorf I M, Weis M R and Gilgenbach R M 2011 *Phys. Rev. E* **83** 066405
[15] Zhang Y and Ding N 2008 *Chin. Phys. B* **17** 2994
[16] Volkov N B, Golub T A, Spielman R B and Gondarenko N A 2001 *Laser Part. Beams* **19** 451
[17] Baksht R B, Fedunin A V, Labetsky A Y, Russkikh A G, Shishlov A V, Diyankov O V, Glazyrin I V and Koshelev S V 1998 *IEEE Trans. Plasma Sci.* **26** 1259
[18] Hammer J H, Eddleman J L, Springer P T, Tabak M, Toor A, Wong K L, Zimmerman G B, Deeney C, Humphreys R, Nash T J, Sanford T W L, Spielman R B and DeGroot J S 1996 *Phys. Plasmas* **3** 2063
[19] Ding N, Zhang Y, Xiao D, Wu J, Dai Z, Yin L, Gao Z, Sun S, Xue C, Ning C, Shu X and Wang J 2016 *Matter Radiat. At. Extremes* **1** 135
[20] Weinwurm M, Bland S N and Chittenden J P 2013 *Phys. Plasmas* **20** 092701
[21] Peterson D L, Bowers R L, Matuska W, McLenithan K D, Chandler G A, Deeney C, Derzon M S, Douglas M, Matzen M K, Nash T J, Spielman R B, Struve K W, Stygar W A and Roderick N F 1999 *Phys. Plasmas* **6** 2178
[22] Chittenden J P, Lebedev S V, Jennings C A, Bland S N and Ciardi A 2004 *Plasma Phys. Control. Fusion* **46** B457
[23] Nash T, Deeney C, Chandler G A, Sinars D B, Cuneo M E and Waisman E M 2004 *Phys. Plasmas* **11** L65
[24] Zier J C, Gilgenbach R M, Chalenski D A, Lau Y Y, French D M, Gomez M R, Patel S G, Rittersdorf I M, Steiner A M, Weis M, Zhang P, Mazarakis M, Cuneo M E and Lopez M 2012 *Phys. Plasmas* **19** 032701
[25] Slutz S A, Herrmann M C, Vesey R A, Sefkow A B, Sinars D B, Rovang D C, Peterson K J and Cuneo M E 2010 *Phys. Plasmas* **17** 056303
[26] Slutz S A and Vesey R A 2012 *Phys. Rev. Lett.* **108** 025003
[27] Sinars D B, Slutz S A, Herrmann M C, *et al.* 2010 *Phys. Rev. Lett.* **105** 185001
[28] McBride R D, Slutz S A, Jennings C A, *et al.* 2012 *Phys. Rev. Lett.* **109** 135004
[29] Sinars D B, Slutz S A, Herrmann M C, *et al.* 2011 *Phys. Plasmas* **18** 056301
[30] Yager-Elorriaga D A, Zhang P, Steiner A M, Jordan N M, Campbell P C, Lau Y Y and Gilgenbach R M 2016 *Phys. Plasmas* **23** 124502
[31] Yager-Elorriaga D A, Zhang P, Steiner A M, Jordan N M, Lau Y Y and Gilgenbach R M 2016 *Phys. Plasmas* **23** 101205
[32] Seyler C E, Martin M R and Hamlin N D 2018 *Phys. Plasmas* **25** 062711
[33] Deng J, Xie W, Feng S, *et al.* 2016 *Matter Radiat. At. Extremes* **1** 48
[34] Douglas M R, Deeney C and Roderick N F 1998 *Phys. Plasmas* **5** 4183
[35] Ofer D, Alon U, Shvarts D, McCrory R L and Verdon C P 1996 *Phys. Plasmas* **3** 3073
[36] Seyler C E and Martin M R 2011 *Phys. Plasmas* **18** 012703
[37] Mignone A, Bodo G, Massaglia S, Matsakos T, Tesileanu O, Zanni C and Ferrari A 2007 *Astrophys. J. Suppl. Ser.* **170** 228
[38] Salzman D 1998 *Atomic Physics in Hot Plasmas* (New York: Oxford University Press) p. 23
[39] Ren X D, Huang X B, Zhou S T, Zhang S Q, Dan J K, Li J, Cai H C, Wang K L, Ouyang K, Xu Q, Duan S C, Chen G H, Wang M, Feng S P, Yang L B, Xie W P and Deng J J 2014 *AIP Conf. Proc.* **1639** 142
[40] Haan S W 1991 *Phys. Fluids B: Plasma Phys.* **3** 2349